Low Lift-to-Drag Morphing Shape Design

Alicia Dwyer Cianciolo[1], Rafael A. Lugo[2], Ashley M. Korzun[2],
Adam C. Slagle[3], Eric M. Queen[2], and Robert A. Dillman[2]
NASA Langley Research Center, Hampton, VA 23681, USA

Richard W. Powell[4]
Analytical Mechanics Associates, Hampton, VA 23666, USA

One advantage of the low lift-to-drag (L/D) inflatable vehicle being evaluated for the human Mars Entry, Descent, and Landing Architecture Study (EDLAS) is the lower launch mass compared to the other concepts being considered. Mass reduction is achieved by using a strong but lightweight inflatable structure and by eliminating the need for a backshell. Performance analysis has shown that additional mass savings is achievable using entry guidance technologies that reduce powered descent propellant mass by directly controlling angle of attack and sideslip, rather than the traditional bank angle control approach used by the current state-of-the-art Mars Science Laboratory entry vehicle. Two methods of implementing this guidance scheme are presented, one uses aerodynamic flaps, the other changes or morphs the shape of the inflatable aeroshell during flight. This paper describes both control methods for the EDLAS low-L/D vehicle, including the aerodynamic model of the aerosurfaces and various methods to achieve the morphing shape deflection (internal motors, shifting tori, etc.). Results of trajectory performance simulations for both the aerodynamic flap and morphing designs are also presented along with details of mechanical implementation options available to ground test the system.

I.   Introduction

Over the past four years, NASA has directed the Entry, Descent and Landing (EDL) Architecture Study (EDLAS) to evaluate candidate technologies to deliver human scale vehicles carrying 20t payloads to the surface of Mars [1,2,3,4]. While several vehicles have been investigated, Phase 3 of the EDLAS (2018-2019) focused on two, a rigid mid lift-to-drag (L/D) vehicle and an inflatable deployable low-L/D vehicle, shown in Table 1. One significant advantage of the low-L/D inflatable vehicle is a lower launch and entry mass compared to the mid-L/D vehicle. The mass reduction is achieved by using a strong but lightweight inflatable forebody structure and eliminating the need for a backshell.

Mars EDL guidance strategies utilizing bank reversals and mass jettisons were successfully demonstrated during the Mars Science Laboratory (MSL) mission in 2012 [5,6] that successfully delivered the rover to 20 km x 7 km preflight estimated landing ellipse. However, to achieve required performance and precision landing capabilities, future crewed Mars entry vehicles, that need to deliver landers within 50 m of a target, will require EDL guidance strategies that go beyond extensions of heritage approaches. Performance analysis has shown that additional mass savings is achievable using entry guidance strategies that directly control angle of attack and sideslip [7], rather than the traditional bank angle control approach used by MSL, to minimize the dispersions at engine initiation thus reducing powered descent propellant mass. This guidance strategy, called Direct Force Control (DFC), can be achieved in a number of methods such as by moving the center of gravity, articulating aerodynamic surfaces similar to airplane control surfaces, or changing or morphing the shape of the inflatable structure during flight.

---

[1] Aerospace Engineer, Atmospheric Flight and Entry Systems Branch, AIAA Senior Member.
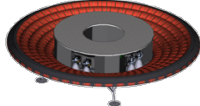[2] Aerospace Engineer, Atmospheric Flight and Entry Systems Branch, AIAA Member.
[3] Aerospace Engineer, Mechanical Systems Branch.
[4] Aerospace Engineer, Analytical Mechanics Associates, AIAA Fellow.

This paper describes the DFC guidance strategy in Section II. A description of the vehicle design and two of the methods to achieve DFC, the aerosurfaces or flaps and the morphing shape, are provided in Section III. The section also provides a description of the aerodynamic model and controller for the morphed shape, (internal motors, shifting tori, etc.). Results of trajectory performance simulations based on the morphing shape model, aerodynamics, and controller are presented in Section IV. As part of the EDLAS Phase 3 goals to identify ground test opportunities for the technologies to enable human scale EDL at Mars, this effort seeks to provide guidelines for a potential ground test opportunity in the future using the 6 m diameter engineering development unit build for the Low-Earth Orbit Flight Test of an Inflatable Decelerator (LOFTID) project [8]. The vehicle implementation is detailed in Section V. Finally, initial analysis indicates that moving mass to achieve the required control authority is not feasible for human-scale Mars vehicles to deliver vehicles to within 50 m of a specified landing target, so this method is not discussed further.

Table 1. EDLAS Phase 3 EDL Vehicle Summary

Name	Shape	Vehicle Dimensions	Launch Mass	Entry Mass	Ballistic Number	L/D
Mid L/D		22 m (l) x 7.3 m (h) x 8.8m (w)	66 t	62 t	380 kg/m^2	0.55
Low L/D		4.3 m (h) x 16 m diameter	57 t	49 t	155 kg/m^2	0.15

II.   Direct Force Control

Traditional Mars entry guidance methods utilize bank angle reversals that rotate the lift vector to mitigate total range and crossrange targeting errors. While proven effective for landing robotic assets (~1 t payload), this approach does not provide sufficient landing accuracy and precision required for crewed and crew support landers (~20 t payload). The finite number of bank reversals limits crossrange error mitigation performance, and the use of the bank angle magnitude for downrange error mitigation results in large landing ellipses, with the longer axis in the downrange direction. The bank reversals are also inherently open loop, meaning that the guidance must wait for the reversal to complete before providing new bank angle commands. Additionally, this approach couples the range errors, since the time, number, and magnitude of bank reversals all affect both the crossrange and downrange errors.

The key advantage of DFC is that it decouples these targeting parameters [7]. Consider a system that permits direct control of angle of attack and angle of sideslip, like a conventional airplane, that uses elevators to control angle of attack and rudders to control angle of sideslip. Similarly, an entry vehicle with the ability to directly control these wind angles would be able to manage landing range errors without requiring bank reversals, given an appropriate guidance scheme. By modulating angle of attack at intervals, the lift vector is adjusted such that the predicted downrange errors at landing may be continuously minimized. Similarly, modulating angle of sideslip permits management of predicted crossrange errors.

Note that DFC use of angle of attack and angle of sideslip channels for downrange and crossrange management is particularly effective for blunt bodies. For slender bodies, angle of attack and angle of sideslip modulation is not decoupled because sideslip angle induces a roll angular acceleration because of the dihedral effect. While other DFC methods may be effective for slender bodies, the present work restricts the use of DFC to blunt bodies. The next section describes the vehicle system used in this study.

EDLAS performance analyses have shown that powered descent (PD) propellant usage can be reduced by using an entry guidance approach that utilizes DFC. For the low-L/D human-scale Mars entry vehicle, DFC can be achieved in a number of ways. Section IV will describe two methods considered, namely articulating aerodynamic surfaces and morphing the shape of the inflatable structure during flight.

III.   Vehicle Systems Modeling

A summary of the low-L/D entry vehicle is provided here; a detailed description of the integrated low-L/D vehicle design is provided in Ref. [4], which is based on smaller inflatable flight vehicle [9] and a manufactured 6 m diameter LOFTID project test article [8]. The test article is scheduled to perform a low Earth orbit (LEO) return in March 2022. The vehicle is composed of four primary components. The first component is the 9.1 m diameter rigid nose cap, or center body, that provides the anchor for the inflatable structure and includes doors or surfaces that open to expose PD engines and landing legs after the entry heat and pressure pulses. The second component is the inflatable structure

that includes five inflatable tori. Each torus has a 0.7 m minor diameter (tube diameter), associated structural webbing, and one torus with a smaller minor diameter and largest major diameter to mitigate shoulder heating. The third component is the inflation system, which includes valves, check valves, inflation manifolds, pressure relief ports, mounting brackets, tubing, adapter fittings, ground servicing connections, and safety lockouts. The inflation gas is nitrogen and the tori are all filled to 19 psi. The tori are covered with a non-ablative flexible thermal protection system that protects the vehicle during entry. An image of the baseline low-L/D vehicle design is shown in Fig. 1. The image does not include the flaps or morphing design, but they are described in the following subsections.
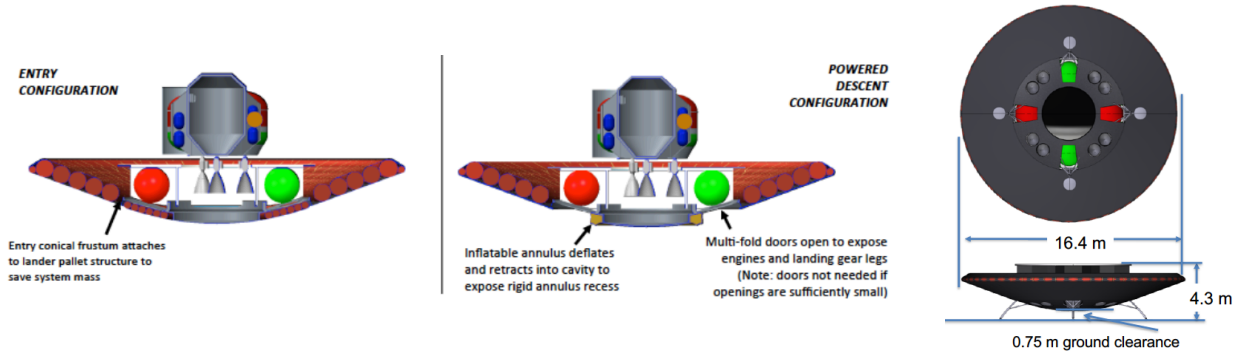

Fig. 1 Baseline low L/D vehicle design showing the entry configuration (left), powered descent configuration (middle) and the landed and forebody configuration (right).

A. Aerodynamic Flaps

For the low-L/D vehicle equipped with deployable, moveable aerodynamic flaps, the flaps are located at the edge of the inflated heat shield at 0°, 90°, 180°, and 270°, as shown in Fig. 2a. While the flap size in the image is notional, the flap size area, deployment angle, and resultant trim characteristics used in the analysis are based on existing ground test data obtained at supersonic and hypersonic conditions [10]. Each individual flap has an aspect ratio of 2:1, with dimensions of 3.62 m by 1.81 m, or 3.11% of the total aerodynamic reference area of the low-L/D vehicle. This results in a flap hinge moment arm of 0.9062 m.
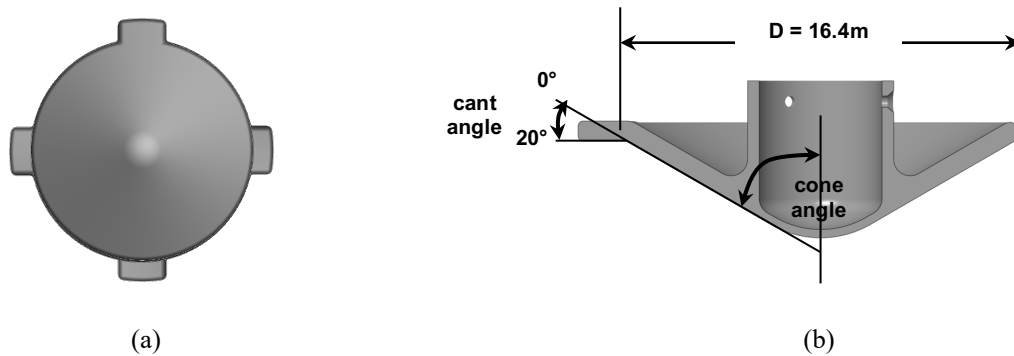

Fig. 2 Aerodynamic flap placement, flap size is notional and not to scale (a). Flap deflection angles (b)

For the purposes of computing the resultant hinge moment, the hinge location for each flap assumes a scaled-up MSL heatshield geometry. Specifically, the flap hinge is placed at the intersection of the largest diameter and the backshell/heatshield separation plane, as shown in Fig. 3a. The flap deployment angles are such that at a command of 0.0, the flap is completely out of the flow (stowed) and does not contribute to the vehicle aerodynamic drag. At maximum deployment, corresponding to a command of 1.0, the flap is angled 20° past the tangential to the 70° sphere-cone heatshield, as shown Fig. 3b. Thus, the total range of flap actuation is 90°.

Controllability analysis determined that a minimum flap rate of 18°/s is sufficient for overall vehicle performance (e.g., < 50 m range error at landing). The flap actuation model assumes instantaneous acceleration. Given a 99%-tile high dynamic pressure of 5.151 kPa, obtained from 3DOF performance Monte Carlo simulations, a fully deployed flap, a vehicle angle of attack of 0° (which maximizes flap exposure), and Newtonian flow approximations for computing the flap pressure coefficient, the resultant hinge moment is 61,297 N-m (524,523 in-lbf). A brief survey

showed that industrial motors exist that are capable providing this moment. The difficulty of mounting and actuating flaps on an inflatable heatshield leads to the investigation of the morphing aeroshell, discussed next.
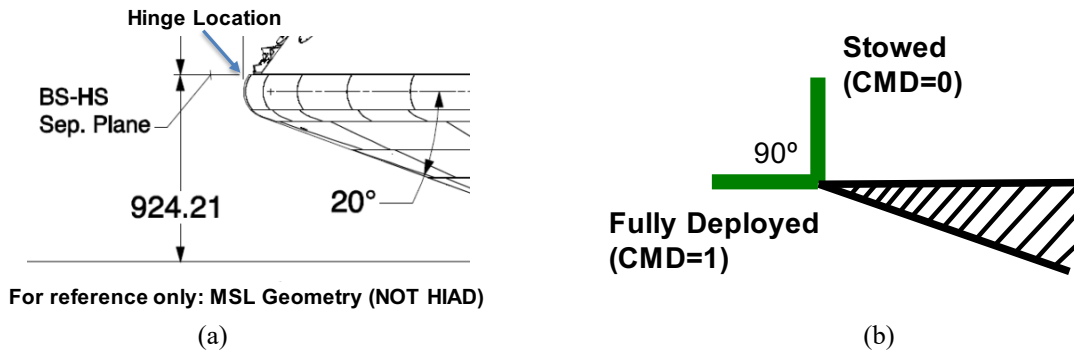

Fig. 3 Flap hinge location (a) and flap deployment range (b).

Controllability analysis determined that a minimum flap rate of 18°/s is sufficient for overall vehicle performance (e.g., < 50 m range error at landing, see Section IV.A). The flap actuation model assumes instantaneous acceleration. Given a 99%-tile high dynamic pressure of 5.151 kPa, obtained from 3DOF performance Monte Carlo simulations, a fully deployed flap, a vehicle angle of attack of 0° (which maximizes flap exposure), and Newtonian flow approximations for computing the flap pressure coefficient, the resultant hinge moment is 61,297 N-m (524,523 in-lbf). A brief survey showed that industrial motors exist that are capable providing this moment. The difficulty of mounting and actuating flaps on an inflatable heatshield leads to the investigation of the morphing aeroshell, discussed next.

B. Aeroshell Morphing

The stiffness of the inflatable structure is designed to support entry loads but is not completely rigid. Two design features permit a morphing shape that enables DFC. The first is the ability to vary the internal torii pressure using the inflation system, and the second is the strap system that holds the tori in place. These features can be designed to permit the vehicle shape to be carefully controlled to generate a non-symmetric aeroshell shape that trims the vehicle to a non-zero angle of attack, generating lift or sideslip. This paper will focus on the option of using actuated straps to enable DFC.

Several morphing shape actuator configurations are considered. The first examined as many as 80 straps anchored to the rigid center body, evenly spaced around the inflatable structure, though additional studies were carried out with as few as 18 straps. The strap design allows for the outer most rim of the inflatable structure to be pulled at any clock angle; see the image in Fig. 4a. The base of the strap system, located on the outer edge of center body, houses a series of independent electric motors spaced equally around the rigid structure. These motors drive high-strength cables secured to a polymeric skin on the outer torus to pull a wedge section of the aeroshell radially inward to generate a non-symmetric shape. Independent motor control permits an assumption of uncoupled angle of attack and sideslip control through the selective actuation and cable length enforcements of the motors. The resulting system is responsive due to the high speed of electric motors and requires minimal changes to the existing low-L/D decelerator design since it directly manipulates the inflatable structure itself. Additionally, this enables the possibility of a continuous control surface over the circumference that permits change in the direction of the lift vector without the fuel expense required by rolling the vehicle using bank reversals. This design, which allows for fine resolution control, allows for pull variability and added control over the width and location of the deflection. However, this design requires many motors and associated lines, power, and mass. Notionally, a coarser system that uses fewer, but larger motors and straps is possible, but this increases the localized loads at the strap-outer torus interface. Work in this area is ongoing.

A second actuator configuration considers a completely decoupled angle of attack and sideslip control using a simplified control system that could be implemented with either coarse or fine resolution. This design assumes primary control along the cardinal axes of the vehicle, minimizing the number of actual actuators, while branching into a larger network of webbed straps that extend to the outer edge of the inflatable structure. An image of the second actuator option is shown in Fig. 4b.
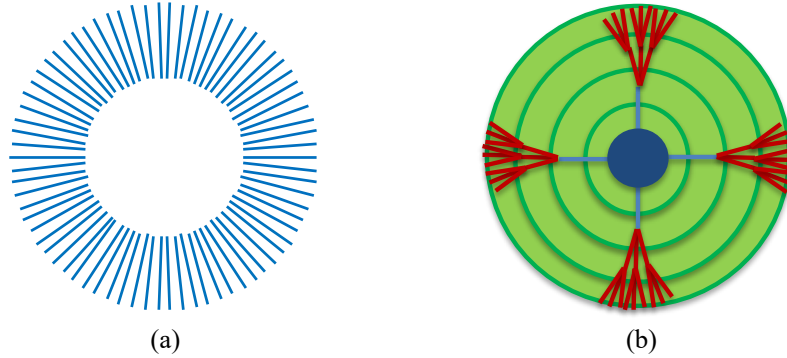
4

(a)   (b)

Fig. 4 Evenly spaced around the inflatable structures (a), decoupled control using less actuators (b).

Initial analysis was performed using the evenly spaced strap configuration to determine the effectiveness of the design. To produce a morphed shape, a series of morphing straps are attached to a finite element low-L/D model, shown in Fig. 5. The structure is first preloaded by pressurizing the tori-stack, and an aerodynamic load is applied to the structure. Straps are pulled in towards the low-L/D center body in a tapered loading pattern such that the maximum displacement occurs at the center of the morphed section, decreasing to zero at the boundaries of the morphed region. Motors on the center body actuate the straps individually. For the analysis, it is assumed that the angle of attack channel does not influence the angle of sideslip channel.

The morphed sections are applied as four control surfaces. Two angle of attack control surfaces spanning 120° wedges are located on opposite sides of the heatshield, along the +z and –z axes. These surfaces are adjusted using 24 morphing straps on each wedge. An image of the +z wedge is shown in Fig. 6. Because less sideslip control is needed to meet performance criteria, two angle of sideslip control surfaces spanning only 60° wedges are located on opposite sides of the heatshield, along the +y and –y axes. These surfaces are each adjusted using 13 morphing straps.

While similar angle of attack and sideslip performance can be achieved using either of the actuator configurations discussed in this section, only one aerodynamics and controller model was developed for the simulation. These are described in the following sections.
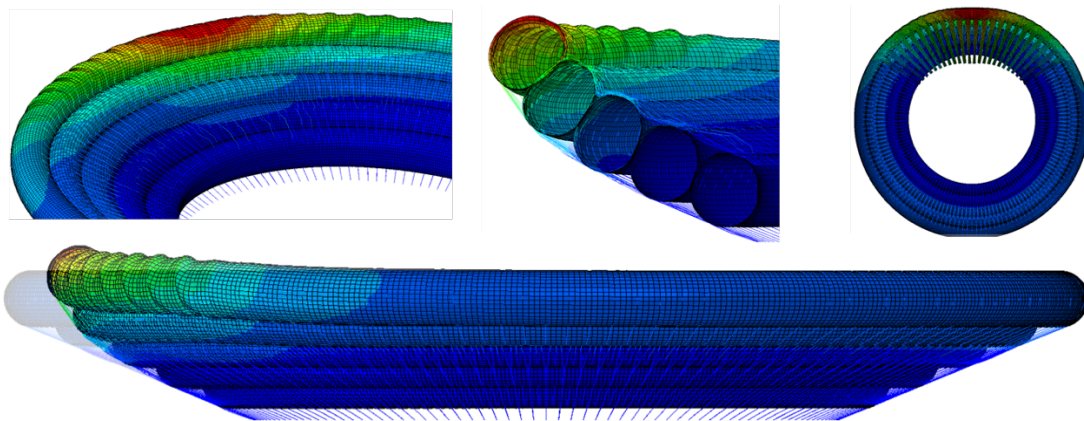

Fig. 5 Morphing low-L/D deformed shape (multiple views).

C. Aerodynamics for Direct Force Control

An extensive aerodynamic database exists for the 70-° sphere-cone shape. Heritage extends to the Viking and more recent Mars robotic missions [10]. Therefore, the aerodynamics model for the morphing shape is composed of the heritage baseline and with changes due to the shape deformation. The changes in aerodynamics are functions of angle of attack, angle of sideslip, deformation from the wedge center (pull angle), and deformation magnitude (pull length). The vehicle trims in the plane of the pull direction (δ in Fig. 6) and pitches the vehicle in the direction opposite of the morphed shoulder region. The aerodynamic response to morphing is based on the 120° wedges for angle of attack control and 60° wedges for sideslip control. Deflection is largest at the center of the wedge and decreases away from the center as depicted in Fig. 6.
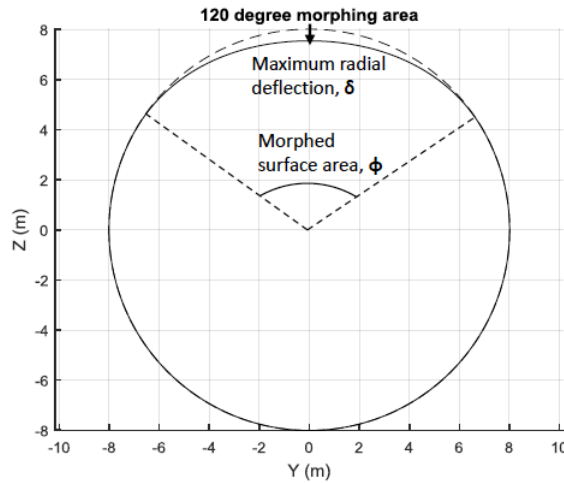
5

Fig. 6 +*z* control surface configuration using 120 deg wedge.

To determine the aerodynamic deflection, LAURA [11] computational fluid dynamic (CFD) solutions were run for a range of angle of attack from 0º to 12º at peak heating and peak dynamic pressure points along the trajectory. Additional Newtonian solutions were generated with the center of the deflected wedge in 15º increments away from the pitch plane, from 0º to 180º. Figure 7 shows LAURA solutions for the vehicle at an angle of attack at 12º. Figure 7a shows the shape with no deformation. Figure 7b shows the effect on the surface pressure distribution when the bottom shoulder is morphed fully. The 120° wedge total distance deflection is 0.43 m demonstrating that relatively small displacements throughout entry generate the required forces needed to achieve DFC. Once the CFD solutions were complete and the differences from the nominal aerodynamic model calculated, the aerodynamic model was implemented in the performance simulation described in Section IV.
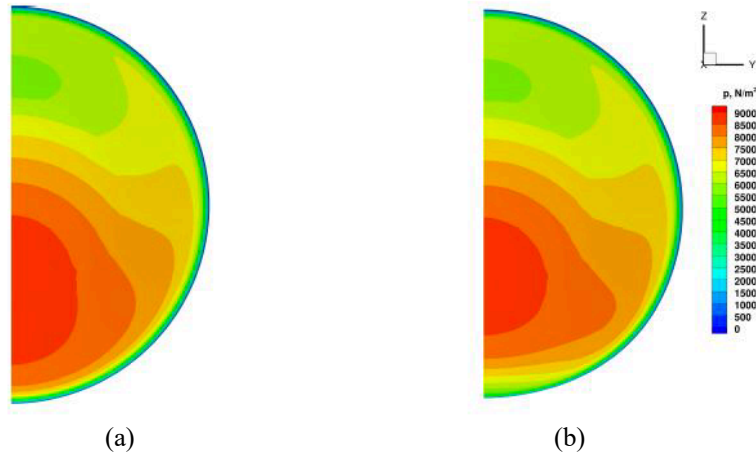

| (a) | (b) |

Fig. 7 Vehicle at 12° angle of attack with no deflection (a) and with 120° wedge angle on the -*z* axis (b).

D. Aerosurface Controller

A simple proportional-integral-derivative (PID) controller was developed to translate the guidance angle of attack and sideslip commands to the aerosurface deflections required to achieve those commands. The controller pitch channel states are angle of attack, integral angle of attack error, and pitch rate. The yaw channel states are angle of sideslip, integral sideslip error, and yaw rate. The current navigated angles of attack and sideslip are obtained from the onboard navigation filter. The same controller is used for both the morphing and flap DFC implementations but with different gains. The gains are scheduled on relative velocity.

In the current formulation, the aerosurface controller treats the angle of attack and sideslip commands as independent channels, assuming that the 0° and 180° aerosurfaces (top and bottom) modulate angle of attack and the 90° and 270° aerosurfaces modulate angle of sideslip. For the morphing aerosurfaces, these are referred to as "pull"

angles. Later assessments will consider continuous pull angles, but in the present work, reducing them to the four cardinal locations permits the use of similar controller algorithms for both the flap and morphing approaches. The cardinal pull angles also preserve the decoupling of pitch and yaw control as commanded by the guidance algorithm.

The commanded aerosurface deflection magnitudes range from 0 (no aerodynamic effect) to 1 (maximum aerodynamic effect). As described in Section III.A., the flaps were rate-limited to 18°/s. This corresponds to a command rate of 20% of total deflection per second. The same 20%/s rate limit was used for the morphing aerosurface, meaning that it takes 5 s to achieve maximum morphing deflection.

In the performance simulation, the onboard guidance uses only the nominal (non-deflected) aerodynamics and therefore does not take into account contributions from the morphing aeroshell or the actuated flaps. Also note that a fully deployed flap increases aerodynamic drag, while a fully morphed wedge decreases aerodynamic drag. Ultimately, the aerodynamic contributions of these aerosurfaces are relatively small, and the guidance is able to compensate.

IV.   Results

This section describes the performance simulation and results of using DFC methods for the low L/D human-scale Mars entry vehicle. A numerical predictor-corrector (NPC) guidance algorithm [12] is implemented in Program to Simulate Optimized Trajectories II (POST2)[13]. The aerodynamics and controller models described in the previous sections are also implemented in the simulation.

A. Requirement, Ground Rules, and Assumptions

Monte Carlo simulations were performed for this analysis. The dispersions listed in Table 2. Other requirements and related statistics used for this analysis are listed in Table 3. Three primary ground rules and assumptions apply. The first is that the simulations initiates at the apoapsis of a one-sol orbit (33,890 km x 250 km) where the vehicle performs an instantaneous deorbit burn. The low L/D entry vehicle has a diameter of 16.4 m and uses eight 100 kN engines for powered descent. The guidance algorithm determines the engine initiation time such that it lands at 0 km above the reference Mars Orbiter Laser Altimeter (MOLA) areoid near the equator.

Table 3. Monte Carlo Dispersions.

Category	Parameter	Dispersion	Distribution
Initial Conditions	Deorbit burn execution	0.135 m/s 3σ	normal
	Uncorrelated state covariance	0.03° 3σ for angles, 0.03 km 3σ for altitudes	normal
Atmosphere	Density	MarsGRAM	--
	Winds	MarsGRAM	--
	Dusttau	0.1:0.9	uniform
Aerodynamics	Aerodatabase uses coefficient multipliers and adders for different aerodynamic regimes based on CFD, wind tunnel tests, and flight data from similar shapes	--	--
Propulsion	Peak thrust	Scale factor: 1% 3σ	normal
	Peak Isp	Scale factor: 1% 3σ	normal
	Start lag time	0.0:0.2 s	uniform
	Startup transient rate	Scale factor: 1% 3σ	normal
	Main phase response rate	Scale factor: 1% 3σ	normal
Mass	Mass	500 kg 3σ	normal
	Center of gravity	0.05 m 3σ	normal
	Moments of inertia	5% kg-m^2 3σ	normal

Table 2. Performance simulation requirements and related statistics.

Requirement	Value	Uncertainty	Statistic
Landed payload	20 t	--	1%-tile
Landed location/total range	Near equator	50 m	99%-tile
Landed altitude	0 km MOLA	±5 m	1%-tile/99%-tile
Landed attitude	Feet-down	±0.1°	1%-tile/99%-tile
Maximum aerodynamic deceleration (10 pt. running mean)	4 g	--	99%-tile
Maximum total angle of attack at SRP initiation	0°	±20°	1%-tile/99%-tile

B. Controller Performance

Nominal morphing controller performance is shown in Fig. 8Fig. and Fig. 9. First, consider the angle of attack channel in Fig. 8. Note the dual y-axes: angle of attack in degrees is on the left and the pull magnitude is on the right. At the moment of G&C initialization (time zero), the navigated and truth angle of attack is just over 1°. The initial guidance command is approximately -6°. The vehicle reference trajectory was deliberately designed to fly at -6° angle of attack in order to exercise the system. Over the course of the first 20 s, the controller commands the morphing wedge at the 0° pull angle. It can be observed that the pull magnitude ramps up from 0 to approximately 0.55, or just over half of the available control authority. After 20 s, the vehicle reaches the commanded angle of attack, and the controller maintains the pull magnitude at approximately 0.55. At approximately 120 s, the guidance commands -7°, and the controller increases its pull magnitude accordingly to 0.6. Thus, it can be concluded that for this nominal trajectory (e.g., no dispersions), there is sufficient control authority using the morphing aerosurfaces.

There is very clear oscillatory, or "ringing" behavior shown in the pull magnitude commands. This is indicative of an over-gained controller, and additional controller tuning must be performed to adequately address this ringing. This also results in the vehicle response oscillating rather than maintaining the commanded steady state. There are also non-zero deflections at the 180° pull angle, which is also an indicator of an over-gained system, as this channel should not be needed to achieve negative angles of attack.
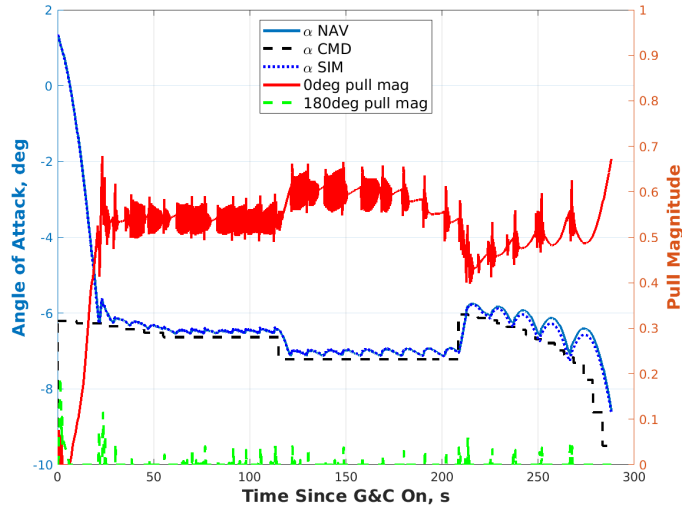

Fig. 8 Controller performance using morphing aerosurfaces in angle of attack channel.

Now consider the angle of sideslip channel shown in Fig. 9. In contrast to the angle of attack channel, the command and vehicle response in this channel is noticeably smoother. This is partially due to the fact that the guidance commands a continuous angle of sideslip command to null out azimuth errors, which directly correlate to crossrange errors at landing [12]. Since the nature of the atmospheric structure tends to be flat layers, the vehicle is less susceptible to atmospheric dispersions in crossrange than downrange. This means that a relatively small angle of sideslip command can clean up large crossrange errors. The controller gains in this channel appear appropriately tuned, as there is little to no ringing as there was in the angle of attack channel, and the pull angle switches from 90° to 270° as the command switches sign, as expected.
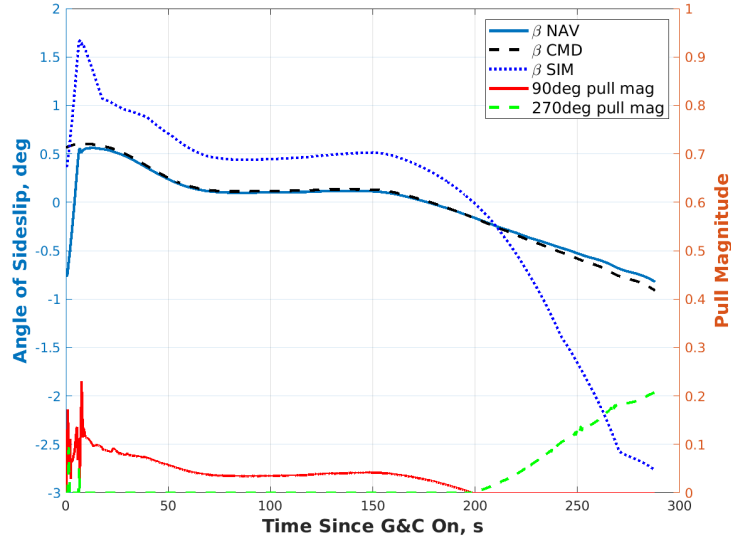
Fig. 9 Controller performance using morphing aerosurfaces in angle of sideslip channel.

The commands and vehicle responses between the morphing and flap DFC approaches are compared in Fig. 10. The flap response (dashed green) is very closely in line with the command (solid red). While the flap-controlled vehicle responds faster to attitude commands, it uses more control authority to do so and has slightly more overshoot. This may be attributed to well-tuned gains for the flap case but may also be attributed to flap performance. Recall from Section II.D. that the flaps increase aerodynamic drag as they are deployed, while a deflected morphing aerosurface decreases aerodynamic drag. This inherently reduces the morphing performance. This also affects the actual command: at approximately 210 s, the flap-controlled vehicle moves to more positive angle of attack (less lift) to avoid overshooting target, whereas the morphing-controlled vehicle angle of attack becomes more negative.
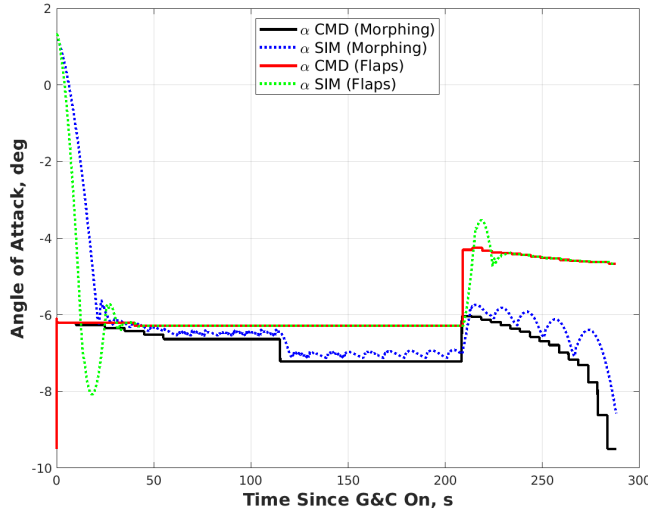

Fig. 10 Comparison between flap and morphing aerosurface commands and responses.

C. Integrated Vehicle Performance

The integrated vehicle performance comparison between the flap- and morphing-controlled cases is shown in Fig. 11. Histograms showing the 8001-case Monte Carlo results for total propellant use and miss distance (i.e., range error at landing) are shown at left and right, respectively. Note that the "Percentage" value listed is the percent of 8001 cases run for each Monte Carlo that landed with a non-zero mass. In the POST2 simulation, a case that does not finish, uses up all propellant and burns all structure, or reaches an angle of attack of 90° during PD, is marked as failed and set a zero mass at landing. These cases are excluded from the histograms. The 99%-tile values are comparable, as is the mean. Overall, the results are very similar. The morphing case shows a few more outliers than the flap case and a

slightly larger variance. This is expected due to similarities in the aerodynamics model and controller models developed for the simulation.
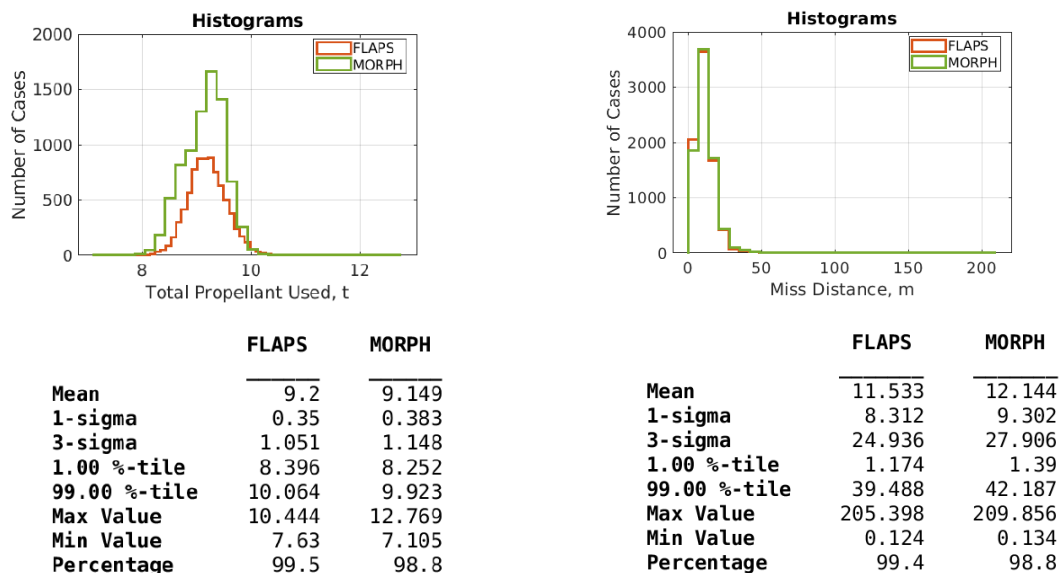

	FLAPS	MORPH			FLAPS	MORPH
Mean	9.2	9.149		Mean	11.533	12.144
1-sigma	0.35	0.383		1-sigma	8.312	9.302
3-sigma	1.051	1.148		3-sigma	24.936	27.906
1.00 %-tile	8.396	8.252		1.00 %-tile	1.174	1.39
99.00 %-tile	10.064	9.923		99.00 %-tile	39.488	42.187
Max Value	10.444	12.769		Max Value	205.398	209.856
Min Value	7.63	7.105		Min Value	0.124	0.134
Percentage	99.5	98.8		Percentage	99.4	98.8

Fig. 11 Integrated performance results of the low L/D human-scale Mars entry vehicle comparison between aerodynamic flaps and morphing aeroshell.

V.   Ground Test

The EDLAS team has secured the 6m LOFTID engineering demonstration unit to design and implement a mechanical system to demonstrate DFC on an inflated forebody. Subsequent analysis in 2020 will determine the details of the mechanical design (e.g., the number of straps, strap design, the type, and number of actuators, etc.) needed to obtain the deflections presented herein. Future work using the demonstration unit will validate deflection performance capability and control models. Eventually, wind tunnel tests or additional CFD will be used to validate the morphed shape aerodynamic model. Issues related to scaling the system to human scale (e.g. 16 m diameter) will be addressed. Once the mechanical implementation and model validation for a morphed shape are complete, efforts to implement the system on a flight test will commence.

VI.   Conclusion

DFC has been shown to provide significant improvements to spacecraft EDL performance and landing accuracy in performance simulations. This paper presented recent analyses to characterize two methods for achieving DFC on a human scale Mars entry vehicle using flaps and morphing the vehicle shape that provide similar performance with respect to propellant used and landed distant from the target. Since the low-L/D vehicle is the lowest mass option being considered for human scale missions, efforts will continue to design and implement DFC methods on small scale demonstration units to determine if the deflection and control authority required to land within human mission constraints is feasible. The goal is to eventually demonstrate a DFC system using a flight test.

References

[1] Cianciolo, A. D. and Polsgrove, T. T., "Human Mars Entry, Descent and Landing Architecture Study Overview," AIAA Paper 2016-5494, Sept. 2016.

[2] Polsgrove,T. T., Thomas, H. D., Cianciolo, A. D., Collins, T., Samareh, J. "Mission and Design Sensitivities for Human Mars Landers Using Hypersonic Inflatable Aerodynamic Decelerators" 2017 IEEE Aerospace Conference, 4-11 March 2017.

[3] Cianciolo, A. D. and Polsgrove, T. T., "Human Mars Entry, Descent and Landing Architecture Study: Phase 2 Summary," AIAA Paper 2018-5190, Sept. 2018.

[4] Cianciolo, A. D., Dillman, R., Brune, Lugo, R. A., Polsgrove, T. T., Percy T. K., Sutherlin, S., A., Johnson, C., and Cassell, A., "Human Mars Entry, Descent and Landing Architecture Study: Deployable Decelerators," AIAA Paper 2018-5191, Sept. 2018.

[5] G. M. Mendeck and L. C. McGrew, "Post-Flight EDL Entry Guidance Performance of the 2011 Mars Science Laboratory Mission," AAS Paper 13-419.

[6] D. W. Way, J. L. Davis, and J. D. Shidner, "Assessment of the Mars Science Laboratory Entry, Descent and Landing Simulation," AAS Paper 13-420.

[7] Cianciolo, A. D., and Powell, R. W. "Entry, Descent, and Landing Guidance and Control Approaches to Satisfy Mars Human Mars Mission Landing Criteria." AAS Paper 17-254.

[8] Dillman, R. A., DiNonno, J. M., Bodkin, R. J., Hughes, S. J., Cheatwood, F. M., Blakeley, H., Akamine, R. L. and Bowes, A. "Planned Orbital Flight Test of a 6m HIAD." International Planetary Probe Workshop, Boulder, CO, 2018.

[9] Olds, A. D., Beck, R., Bose, D., White, J., Edquist, E., Hollis, B., Lindell, M., and Cheatwood, F. N., "IRVE-3 Post Flight Reconstruction." AIAA-2013-3398.

[10] Korzun, A. M., Murphy, K. J., Edquist, K. T., "Supersonic Aerodynamic Characteristics of Blunt Body Trim Tab Configurations", AIAA 2013-2809, June 2013.

[11] Mazaheri, A., Gnoffo, P., Johnston, C.O., Kleb, W. L. "LAURA User's Manual: 5.5-64987", NASA/TM-2013-217800.

[12] Lugo, R. A., and Powell, R. W., "Overview of a Generalized Numerical Predictor-Corrector Targeting Guidance with Application to Human-Scale Mars Entry, Descent, and Landing," AIAA SciTech 2020 Abstract Accepted.

[13] R. A. Lugo, J. D. Shidner, R. W. Powell, S. M. Marsh, J. A. Hoffman, D. K. Litton, and T. L. Schmitt, "Launch Vehicle Ascent Trajectory Simulation using the Program to Optimize Simulated Trajectories II (POST2)," AAS Paper 17-274.